nature geoscience

ARTICLES

https://doi.org/10.1038/s41561-018-0286-2

Disproportionately strong climate forcing from extratropical explosive volcanic eruptions

Matthew Toohey[1]*, Kirstin Krüger[2], Hauke Schmidt[3], Claudia Timmreck[3], Michael Sigl[2,4,5], Markus Stoffel[6,7,8] and Rob Wilson[9,10]

Extratropical volcanic eruptions are commonly thought to be less effective at driving large-scale surface cooling than tropical eruptions. However, recent minor extratropical eruptions have produced a measurable climate impact, and proxy records suggest that the most extreme Northern Hemisphere cold period of the Common Era was initiated by an extratropical eruption in 536 CE. Using ice-core-derived volcanic stratospheric sulfur injections and Northern Hemisphere summer temperature reconstructions from tree rings, we show here that in proportion to their estimated stratospheric sulfur injection, extratropical explosive eruptions since 750 CE have produced stronger hemispheric cooling than tropical eruptions. Stratospheric aerosol simulations demonstrate that for eruptions with a sulfur injection magnitude and height equal to that of the 1991 Mount Pinatubo eruption, extratropical eruptions produce time-integrated radiative forcing anomalies over the Northern Hemisphere extratropics up to 80% greater than tropical eruptions, as decreases in aerosol lifetime are overwhelmed by the enhanced radiative impact associated with the relative confinement of aerosol to a single hemisphere. The model results are consistent with the temperature reconstructions, and elucidate how the radiative forcing produced by extratropical eruptions is strongly dependent on the eruption season and sulfur injection height within the stratosphere.

Major volcanic eruptions impact climate through the injection of sulfur into the stratosphere, which increases the abundance of stratospheric sulfate aerosol and its capacity to scatter incoming solar radiation and cool the Earth's surface[1]. The climatic impact of any eruption depends on the properties of the stratospheric aerosol enhancement, and is tied principally to the amount of sulfur injected, but also to the aerosol's atmospheric lifetime, spatial spread and size distribution.

It is commonly thought that extratropical eruptions have a weaker climatic impact than tropical eruptions[2,3]. This hypothesis rests on the idea that aerosol from tropical eruptions spreads globally, and has a longer stratospheric lifetime due to a longer transport path from the tropics to removal across the mid- or high-latitude tropopause[4]. Shorter lifetimes for stratospheric aerosol from extratropical eruptions have been assumed in prior volcanic forcing reconstructions[5,6] and are thus implicit in model studies that support the idea of weaker climate forcing from extratropical eruptions[4].

Comparing the aerosol clouds and climate impacts that result from tropical versus extratropical eruptions based on observations and proxy records is complicated by a number of confounding factors. During the satellite era, stratospheric sulfur injections from the strongest extratropical eruptions were an order of magnitude weaker than the largest tropical eruptions[7]. On longer timescales, ice cores record sulfate from major eruptions from both the tropics and extratropics[8], but limited knowledge of the height of the volcanic sulfur injection from those eruptions adds uncertainty to the estimates of radiative forcing from ice cores[9].

Interest in extratropical eruptions has recently increased due, in part, to a series of minor extratropical volcanic eruptions that produced significant radiative forcing on the climate, which counteracted a portion of greenhouse gas warming[10,11]. Furthermore, model results suggest the hemispherically asymmetric radiative forcing from extratropical eruptions has distinct impacts on tropical precipitation[12,13] and atmospheric and ocean circulation[14,15]. Reconstructions of volcanic activity spanning the past 2,500 years from ice cores have identified large extratropical volcanic events with associated large-scale cooling[8], which include extreme Northern Hemisphere cold conditions initiated by an extratropical eruption around the year 536 CE (refs. [8,16,17]). These findings motivate a re-examination of the radiative forcing and climate impacts of extratropical eruptions.

Summer cooling by tropical and extratropical eruptions

Reconstructions of Northern Hemisphere extratropical summer temperatures over land from tree rings show a clear cooling response to volcanic eruptions[18]. Here we examine the magnitude of the cooling recorded in three tree ring Northern Hemisphere temperature reconstructions[19–21] over the 750–2000 CE period, supplemented with estimates of the eruption region and volcanic stratospheric sulfate injection (VSSI) deduced from ice core sulfate records[22]. We selected eruptions with VSSI > 2 TgS, and excluded cases potentially affected by prior eruptions (Methods and Supplementary Table 1) and five events linked to Iceland (Supplementary Table 2).

Post-volcanic three-year mean Northern Hemisphere temperature anomalies, averaged over the three reconstructions ($\Delta T_{3\mathrm{yr}}^{\mathrm{ALL}}$; Methods), show a clear relationship with VSSI (Fig. 1). Tropical eruptions show a particularly coherent correlation ($r = -0.68$) between temperature and VSSI. Clearly, there is also a scatter in the

---

[1]GEOMAR Helmholtz Centre for Ocean Research Kiel, Kiel, Germany. [2]Department of Geosciences, University of Oslo, Oslo, Norway. [3]Max Planck Institute for Meteorology, Hamburg, Germany. [4]Laboratory of Environmental Chemistry, Paul Scherrer Institute, Villigen, Switzerland. [5]Oeschger Centre for Climate Change Research, Bern, Switzerland. [6]Climate Change Impacts and Risks in the Anthropocene (C-CIA), Institute for Environmental Sciences, University of Geneva, Geneva, Switzerland. [7]dendrolab.ch, Department of Earth Sciences, University of Geneva, Geneva, Switzerland. [8]Department F.-A. Forel for Aquatic and Environmental Sciences, University of Geneva, Geneva, Switzerland. [9]School of Earth and Environmental Sciences, University of St Andrews, Fife, UK. [10]Lamont-Doherty Earth Observatory, Columbia University, Palisades, NY, USA. *e-mail: mtoohey@geomar.de

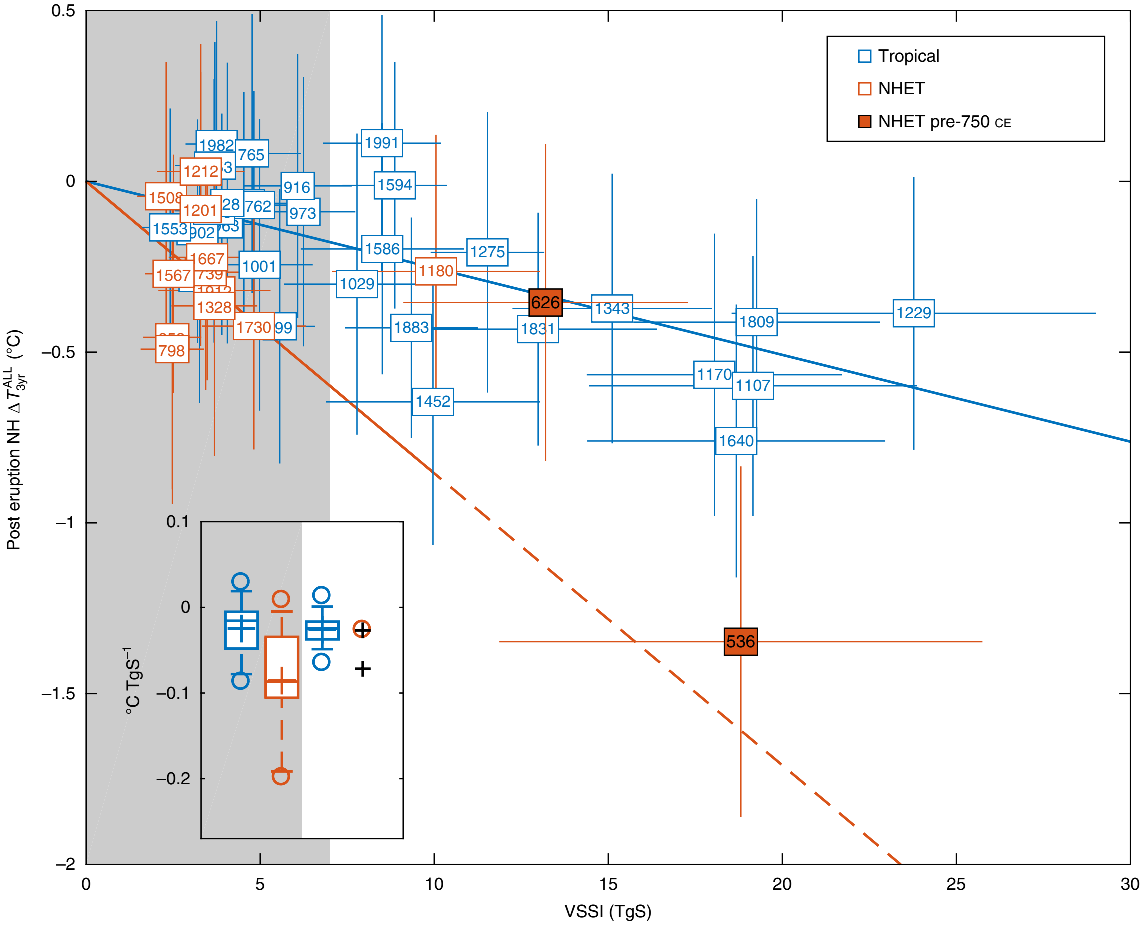

Fig. 1 | Reconstructed post-volcanic Northern Hemisphere temperature response to Northern Hemisphere extratropical and tropical eruptions in relation to VSSI. Three-year mean temperature anomalies (ΔT_{3yr}^{ALL}) are plotted versus the estimated VSSI (TgS) for tropical (blue) and Northern Hemisphere extratropical (NHET; orange) explosive eruptions. Number labels indicate the eruption years. Vertical and horizontal error bars represent ±1σ uncertainties. The 1257 Samalas eruption (Supplementary Table 4) lies outside the chosen limits of the plot. Coloured lines indicate the mean ΔT/VSSI ratio for both tropical and extratropical eruptions after 750 CE. Temperature anomalies for extratropical events before 750 CE are shown with orange-filled markers. Inset shows box plots of the distribution of three-year mean temperature anomalies per unit VSSI for eruptions with VSSI less than 7 TgS (grey background) and greater than 7 TgS (white background). Crosses denote the distribution mean, horizontal lines the median, boxes the 25–75% interquantile range, whiskers the 1–99% interquantile range and outliers are marked with circles. For extratropical eruptions with VSSI > 7 TgS, markers show the ΔT/VSSI ratios for individual eruptions post-750 CE (orange) and pre-750 CE (black).

relationship between ΔT_{3yr} and VSSI, which could be due to uncertainties in both quantities, but also to the influences of internal climate variability on ΔT_{3yr} and the impact of secondary eruption characteristics, such as eruption season and plume height. Ratios of temperature response to VSSI (Fig. 1 inset and Supplementary Tables 4 and 5) show a broad range of values, with outliers that include events with apparent post-eruption warming and very strong apparent cooling. On average, tropical and extratropical eruptions lead to ΔT/VSSI ratios of −0.025 ± 0.005 °C TgS^{-1} and −0.080 ± 0.018 °C TgS^{-1}, respectively (Table 1). The difference between the ΔT/VSSI ratios for extratropical and tropical eruptions is significant at the 99% level ($P = 0.006$)—a factor of roughly 2–4 difference is consistent across the three Northern Hemisphere temperature reconstructions (Table 1 and Supplementary Fig. 1).

The stronger temperature response per unit VSSI to extratropical eruptions is based on a sample of extratropical eruptions with VSSI mostly limited to values less than 7 TgS (Supplementary Table 4). Although this limits the comparability of the temperature responses to extratropical and tropical eruptions, the mean ΔT/VSSI ratios for tropical eruptions are consistent between eruptions less than and greater than 7 TgS (Fig. 1 inset), which suggests that the stronger ΔT/VSSI ratios seen for extratropical eruptions are probably representative. The ΔT/VSSI ratio for extratropical eruptions after 750 CE is consistent with the strong cooling estimated for the 536 CE eruption, albeit from a single reconstruction (Fig. 1 and Supplementary Table 5). However, the extratropical eruptions of 626 and 1180 CE produce ΔT/VSSI ratios on a par with tropical eruptions.

One pertinent issue in the calculation of ΔT/VSSI ratios is uncertainty in the methods used to calculate VSSI, which apply a smaller transfer function for extratropical eruptions than for tropical eruptions in the estimation of volcanic aerosol from ice core sulfate[22,23]. Nonetheless, if VSSI values for extratropical eruptions are calculated as for tropical eruptions, extratropical eruptions still produce an 81% stronger average ΔT/VSSI ratio than tropical eruptions (Table 1).

As aerosol from extratropical eruptions is largely contained within the hemisphere of the eruption[24], whereas that from tropical eruptions spreads globally, a factor of two difference between ΔT/VSSI ratios for extratropical and tropical eruptions could be explained by a relatively equal temperature response to hemispheric aerosol loading, irrespective of latitude of injection. This explanation, however, seemingly contradicts the expectation

Table 1 | Hemispheric temperature anomaly/VSSI ratios for tropical and Northern Hemisphere extratropical explosive eruptions

	N-TREND	STO15	SCH15	ALL
$\left.\frac{\Delta T}{\mathrm{VSSI}}\right\vert_{\mathrm{trop}}$ (°C TgS^{-1})	−0.019 ± 0.006	−0.036 ± 0.009	−0.021 ± 0.003	−0.025 ± 0.005
$\left.\frac{\Delta T}{\mathrm{VSSI}}\right\vert_{\mathrm{extrop}}$ (°C TgS^{-1})	−0.081 ± 0.020	−0.102 ± 0.024	−0.059 ± 0.018	−0.080 ± 0.018
$\left.\frac{\Delta T}{\mathrm{VSSI}}\right\vert_{\mathrm{extrop}} - \left.\frac{\Delta T}{\mathrm{VSSI}}\right\vert_{\mathrm{trop}}$ (%)	330 ± 150	180 ± 82	180 ± 94	220 ± 85
$\left.\frac{\Delta T}{\mathrm{VSSI}^*}\right\vert_{\mathrm{extrop}} - \left.\frac{\Delta T}{\mathrm{VSSI}}\right\vert_{\mathrm{trop}}$ (%)	150 ± 87	58 ± 47	61 ± 54	81 ± 48

Mean ΔT/VSSI values over the tropical ('trop') and extratropical ('extrop') events listed in Supplementary Tables 4 and 5, with 1σ s.e. of the mean are listed for the N-TREND[19], STO15[20] and SCH15[21] Northern Hemisphere temperature reconstructions, along with that from the composite mean of the three reconstructions (ALL). Percent differences between mean extratropical and tropical ΔT/VSSI values are listed with 1σ uncertainties. Percent differences between mean extratropical and tropical ΔT/VSSI values are repeated in the final row with VSSI for extratropical eruptions adjusted (VSSI* = VSSI/0.57) such that the scaling from ice core sulfate flux to VSSI is the same for both tropical and extratropical eruptions.

of a significantly reduced stratospheric aerosol lifetime for extratropical eruptions.

The lifetime of volcanic stratospheric sulfur

To investigate the impact of eruption latitude on the volcanic stratospheric sulfate aerosol evolution we performed ensemble simulations with the coupled aerosol–atmospheric general circulation model MAECHAM5-HAM (Methods). All the simulations include a stratospheric injection of 8.5 TgS, consistent with satellite-based estimates of the 1991 Pinatubo eruption[25], with eruptions in both January and July to include the effect of season[20,26,27]. A set of four eruption latitudes were chosen based on maxima in the latitudinal distribution of identified eruptions within the Volcanoes of the World database[28] (Supplementary Fig. 2), and simulations (Supplementary Table 6) were performed with SO_2 injected at each latitude and 30 hPa (~24 km), consistent with the 1991 Pinatubo eruption. Eruptions at 56° N were also performed with injections into the lower stratosphere at 100 hPa (~16 km) and 150 hPa (~13 km), roughly consistent with the range of estimates[7] of the injection heights of recent minor (VSSI < 1 TgS) extratropical eruptions, which include Kasatochi (2008, 52° N) and Sarychev (2009, 48° N).

The simulated spatiotemporal evolution of volcanic aerosol burden (Fig. 2a–d and Supplementary Fig. 3) shows the global spread of aerosol after tropical eruptions and the hemispheric containment of aerosol for extratropical eruptions. These patterns of aerosol spread are consistent with prior simulations[24], comparisons of tropical versus extratropical temperature reconstructions[29] and our understanding of the general features of large-scale circulation within the stratosphere[30].

For sulfur injections at a fixed height of 30 hPa, the global mean sulfate mass burdens show sensitivity to both the injection latitude and season (Fig. 2e,f). For January (that is, the Northern Hemisphere winter) eruptions, extratropical eruptions produce sulfate burdens that are similar to tropical eruptions, with stratospheric e-folding lifetimes (see Methods) only ~10% smaller (Fig. 2g). For July (that is, the Northern Hemisphere summer) eruptions, global sulfate burdens from extratropical eruptions reach maxima similar to those from tropical eruptions, but decay faster, with lifetimes 24–44% shorter.

Simulations of sulfur injections at 56° N with varying injection heights show that the injection height within the stratosphere plays an important role in controlling the lifetime of stratospheric sulfate. The lifetimes of stratospheric sulfur for extratropical injections at 100 hPa and 150 hPa are notably shorter than those from both tropical and extratropical 30 hPa injections (Fig. 2g). These results can be understood as arising from differences in the transport processes between the lowermost stratosphere (LMS) and 'overworld'[31]. In the LMS, defined as the region between the tropopause and the 380 K potential temperature surface, large-scale two-way transport along potential temperature isentropes exchanges air between the troposphere and stratosphere, whereas in the overworld, isentropes do not cross the tropopause and therefore transport simply redistributes mass within the stratosphere. Sulfate aerosol that results from simulated sulfur injection into the LMS is transported into the troposphere and deposited to the surface rapidly after the injection (Supplementary Fig. 4), whereas the cross-tropopause transport of sulfur injected into the extratropical stratospheric overworld only proceeds after aerosol has descended into the LMS, which prolongs the aerosol lifetime.

Global mean aerosol properties and radiative forcing

The radiative impact of stratospheric aerosol depends not only on its mass, but also on its size distribution[32], because stratospheric sulfate aerosol has a maximum scattering efficiency at an effective radius of ~0.2 μm, with decreasing efficiency for the larger effective radii observed after major eruptions[33,34]. Sulfate-mass-weighted mean effective radius ($\langle r_{\mathrm{eff}}\rangle$; Methods) and global mean stratospheric aerosol optical depth (SAOD) are shown in Fig. 3 as a function of injection location. The simulated effective radius shows sensitivity to eruption latitude, season and injection height (Fig. 3a,b). For January 30 hPa injections, the evolution of $\langle r_{\mathrm{eff}}\rangle$ is similar for extratropical and tropical eruptions, with a peak $\langle r_{\mathrm{eff}}\rangle$ of around 0.4 μm. For July 30 hPa injections, simulated $\langle r_{\mathrm{eff}}\rangle$ for extratropical eruptions reaches much larger values (>0.6 μm) than comparable tropical eruptions (~0.4 μm). Sulfur injections into the extratropical lower stratosphere (100 and 150 hPa) result in a lower $\langle r_{\mathrm{eff}}\rangle$ compared to 30 hPa injections, with, again, July eruptions leading to larger $\langle r_{\mathrm{eff}}\rangle$ values than January eruptions. The sensitivity of $\langle r_{\mathrm{eff}}\rangle$ to eruption latitude, season and injection height can be understood to be primarily controlled by the availability of hydroxyl radical (OH), which controls the rate of SO_2-to-H_2SO_4 conversion. Higher OH values, which occur in the high-latitude stratosphere during summer (Supplementary Fig. 5), lead to faster H_2SO_4 production. When H_2SO_4 production is fast compared to stratospheric mixing and transport processes, H_2SO_4 concentrations are relatively enhanced at a local-to-regional scale, which promotes aerosol growth through condensation and coagulation.

SAOD at 550 nm quantifies the attenuation of solar radiation by aerosol, and is a function of the sulfate burden as well as effective radius. January extratropical 30 hPa injections lead to a global mean SAOD (Fig. 3c) very similar to the tropical 30 hPa eruptions, which reflects similar global sulfate burdens and $\langle r_{\mathrm{eff}}\rangle$. July extratropical 30 hPa injections lead to a much weaker global mean SAOD than tropical 30 hPa eruptions (Fig. 3d), due to both the faster decay of the sulfate burden and larger $\langle r_{\mathrm{eff}}\rangle$. In terms of the three-year cumulative SAOD (Fig. 3e), extratropical 30 hPa injections in January produce only ~10% less global mean SAOD than the comparable tropical eruptions, whereas extratropical 30 hPa eruptions in July produce 30% (36° N) to 53% (56° N) less SAOD compared to the tropical counterparts. In general, injections into the extratropical

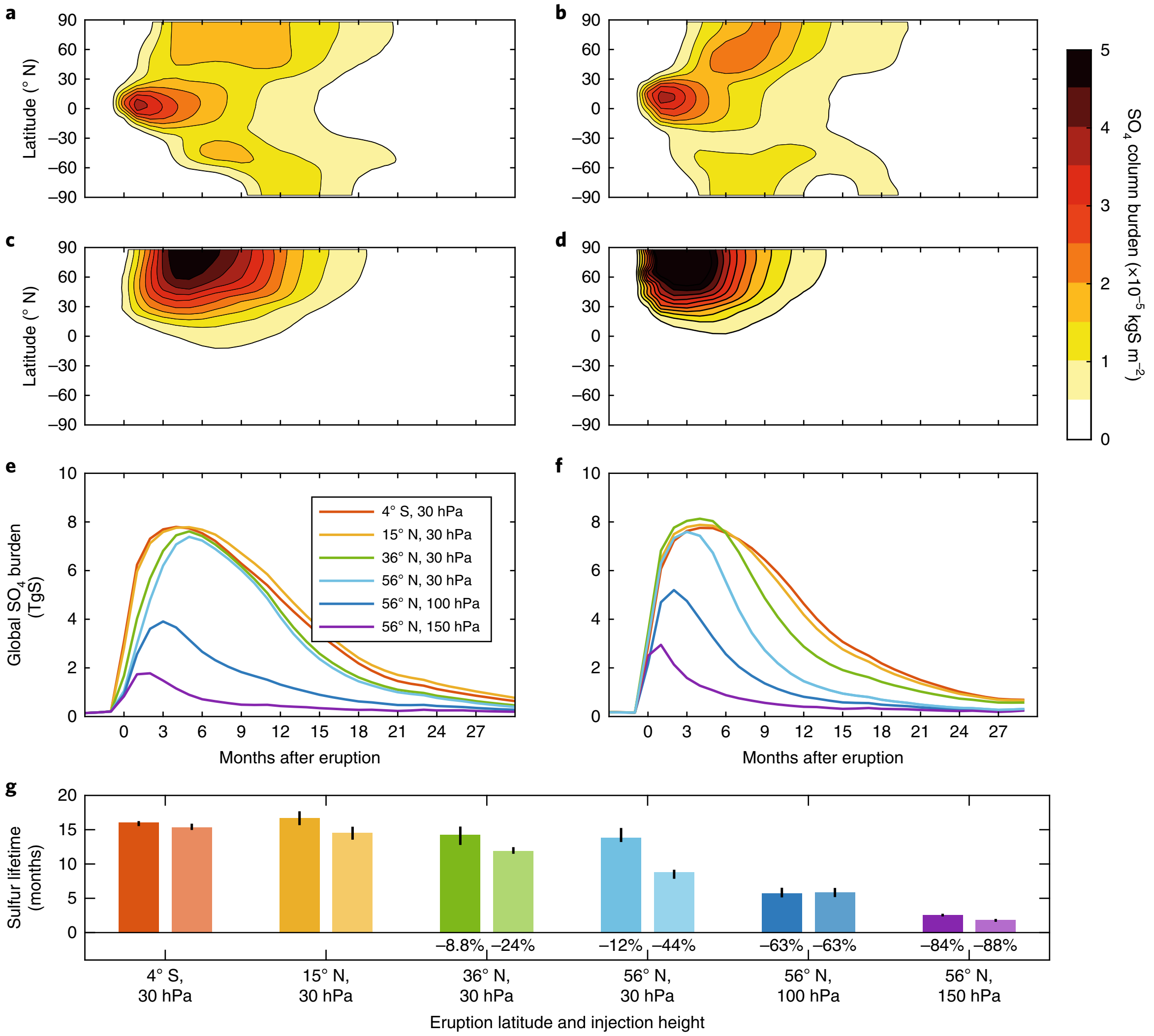

Fig. 2 | Simulated volcanic stratospheric aerosol burdens and lifetimes for varying eruption latitude, season and injection height. a–d, Ensemble mean zonal mean aerosol burdens (kgS m^{-2}) are shown for tropical (15° N) (**a**,**b**) and extratropical (56° N) (**c**,**d**) eruptions of 8.5 TgS in January (**a**,**c**) and July (**b**,**d**) at 30 hPa. **e**,**f**, Ensemble mean global sulfur burden (TgS) time series for the six simulated injection locations in January (**e**) and July (**f**). **g**, Stratospheric sulfur e-folding lifetimes are shown for each eruption latitude and injection height, and the black whiskers indicate the full ensemble spread (darker shade, January; lighter shade, July). For the extratropical injection cases, text labels show the percent difference of sulfur lifetime with respect to the mean of the tropical (4° S and 15° N, 30 hPa) injection eruption simulations.

lower stratosphere lead to smaller SAODs than injections to 30 hPa, although due to the smaller $\langle r_{\mathrm{eff}} \rangle$ for lower injection heights, the impact of the injection height is weaker on SAODs than on sulfate burden lifetimes. The importance of $\langle r_{\mathrm{eff}} \rangle$ is especially apparent for July eruptions at 56° N, for which the simulated peak and cumulative SAOD that result from an 100 hPa injection is similar to that from a 30 hPa injection, despite a smaller sulfate burden.

Postvolcanic surface temperature anomalies result from the impact of aerosol on atmospheric radiative transfer, which is often quantified as radiative forcing (W m^{-2}). The radiative impact of the simulated eruptions is quantified through the top-of-atmosphere net radiative anomalies: as the simulations are performed with fixed sea surface temperatures (SSTs) and sea ice, this is equivalent to the 'fixed SST' version of effective radiative forcing (ERF)[35,36]. Simulated global mean ERF anomalies for extratropical eruptions (Supplementary Fig. 6) at 30 hPa are smaller than those of the corresponding tropical eruptions in the ensemble mean, although this difference is as small as 15%, and in many cases the ensemble range for extratropical eruptions overlaps with that of tropical eruptions. Global mean ERF anomalies for extratropical LMS injections range from 57 to 91% smaller than for tropical eruptions.

Extratropical impact of volcanic radiative forcing

Modelling studies suggest that regional surface temperature responses to external radiative forcing depend on the structure of the forcing, and that Northern Hemisphere extratropical temperatures respond predominantly to extratropical forcing[37]. As the Northern Hemisphere tree-ring-based temperature reconstructions explored above are based on samples collected in the mid-to high latitudes, we examine the simulated radiative forcing in the Northern Hemisphere extratropics (NHET = 30–90° N).

Aerosol from extratropical eruptions is heavily concentrated within the Northern Hemisphere (Fig. 2), and particularly within the NHET where SAODs that results from extratropical 30 hPa eruptions peak at values up to 2–3 times larger than those of tropical 30 hPa injections (Fig. 4a,b). As a result, NHET-averaged ERF (Fig. 4c,d) from extratropical 30 hPa injections is stronger than that from tropical 30 hPa injections. Three-year cumulative

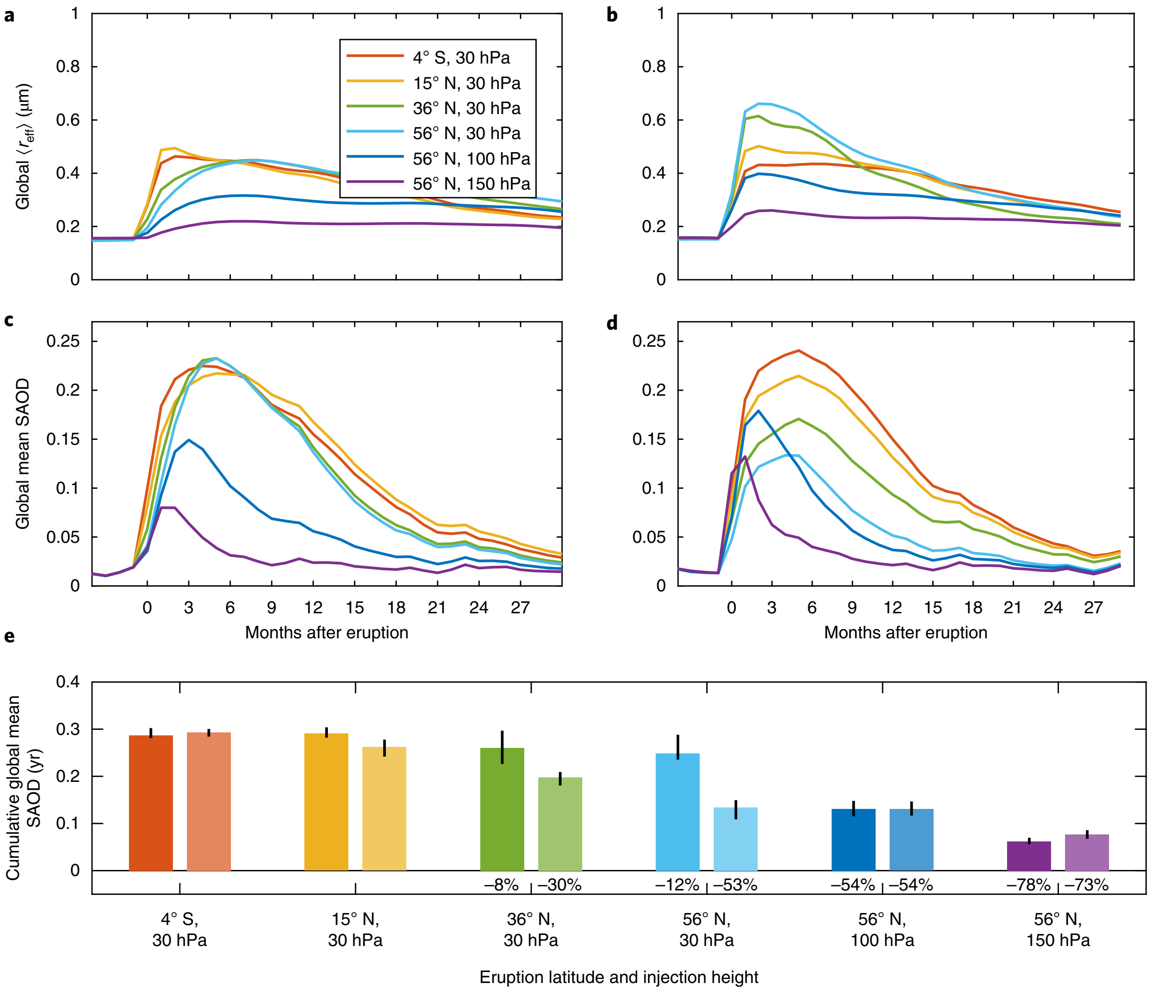

Fig. 3 | Simulated global mean volcanic aerosol properties for varying eruption latitude, season and injection height. **a**–**d**, Ensemble mean $\langle r_{\mathrm{eff}} \rangle$ (**a**,**b**) and SAOD (**c**,**d**) from simulated eruptions of 8.5 TgS in January (**a**,**c**) and July (**b**,**d**). **e**, Three-year cumulative SAOD as a function of injection latitude and height (darker shade, January; lighter shade, July). Black whiskers indicate the full ensemble spread. For the extratropical injection cases, text labels show the percent difference of cumulative SAOD with respect to the mean of the tropical (4° S and 15° N, 30 hPa) injection eruption simulations.

NHET-averaged ERF (Fig. 4e) from extratropical 30 hPa January injections are 70–80% stronger than the average of tropical 30 hPa injections. Extratropical 30 hPa July injections, in contrast, produce cumulative NHET-averaged ERF of −3 to +34% compared to tropical eruptions, which indicates a strong sensitivity to the eruption season. Differences between tropical and extratropical injections are also apparent in the time evolution of ERF: for January eruptions (Fig. 4c), peak ERF values for tropical 30 hPa and extratropical lower stratosphere injections occur within the first four months, whereas ERF for extratropical 30 hPa injections peaks six months after the eruption during the Northern Hemisphere summer. For July eruptions (Fig. 4d), the peak forcing from extratropical injections occurs within the summer of the eruption, whereas that of tropical 30 hPa injections occurs 6–9 months later, during the Northern Hemisphere winter and spring.

Results described above challenge the perception that extratropical eruptions are less climatically important than tropical eruptions. Although simulated SAOD and ERF are weaker for Northern Hemisphere extratropical eruptions than for tropical eruptions in the global mean, the hemispheric confinement of aerosol results in stronger radiative anomalies over the Northern Hemisphere, with NHET ERF for extratropical eruptions up to 80% stronger than tropical eruptions. This result is consistent with the stronger ΔT/VSSI ratio for extratropical eruptions in tree-ring-based Northern Hemisphere temperature reconstructions. Although the tree rings imply a stronger difference between ΔT/VSSI ratios for extratropical and tropical eruptions than the model-based differences in radiative forcing, an 80% stronger response to extratropical eruptions lies within the 2σ uncertainty range of the percent differences in theΔT/VSSI ratio between extratropical and tropical eruptions. Furthermore, quantitative differences between tree-ring-based ΔT/VSSI ratios and model-based radiative forcing may reflect non-linearity in the temperature sensitivity to spatially inhomogeneous radiative forcing[38] and uncertainties in the proxy-based estimates. We note particularly that the quantitative agreement between ΔT/VSSI ratios and the modelled radiative forcing is much closer if the VSSI values for extratropical eruptions were calculated using the same transfer function as for tropical eruptions (Table 1).

Implications for past and future extratropical eruptions

Past reconstructions of volcanic forcing have assumed short stratospheric lifetimes and weak radiative forcing of aerosol from extratropical eruptions. Our modelling experiments confirm a shorter aerosol lifetime for extratropical injections, but for a constant injection height in the stratospheric overworld, the effect is as little as 10%. Our simulations demonstrate that the lifetime of stratospheric aerosol from extratropical injections is strongly connected to the injection height within the stratosphere. The assumption of a short

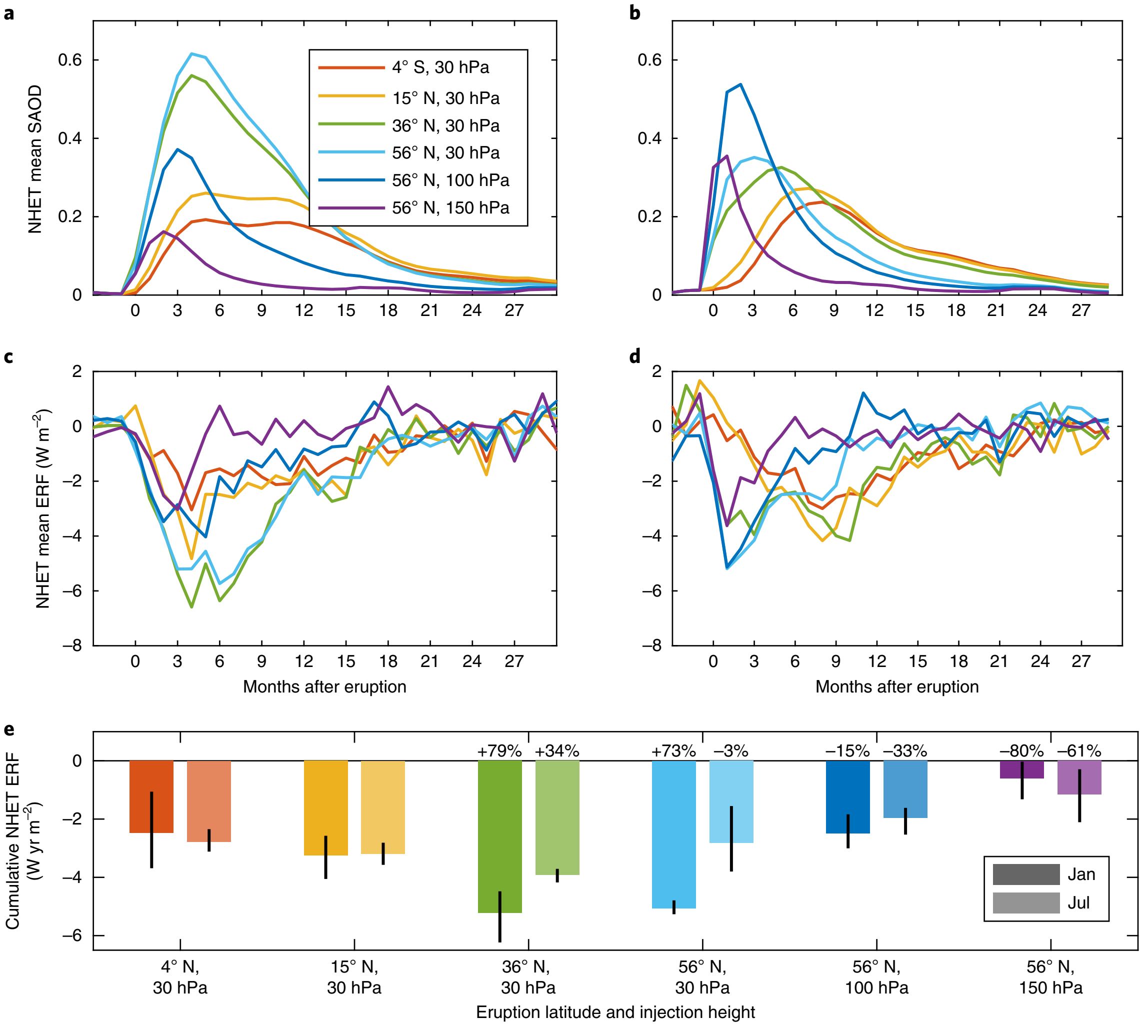

Fig. 4 | Simulated volcanic SAOD and ERF over the NHET for varying eruption latitude, season and injection height. a–d SAOD (**a**,**b**) and ERF (**d**,**e**) for simulated eruptions of 8.5 TgS in January (**a**,**c**) and July (**b**,**d**). **e**, Three-year cumulative NHET ERF as a function of injection latitude and height (darker shade, January; lighter shade, July). Black whiskers indicate the full ensemble spread. For the extratropical injection cases, text labels show the percent difference of cumulative ERF with respect to the mean of the tropical (4° S and 15° N, 30 hPa) injection eruption simulations.

lifetime for extratropical eruptions in previous work[4] is probably tied to an implicit assumption of lower injection heights. However, volcanic plume models suggest that plume heights have a weak dependence on eruption latitude[39,40], and estimated maximum plume heights for the 1912 Katmai (58° N) eruption based on estimated mass eruption rates and tephra dispersal reach 28 km (ref. [41]), comparable to that of Pinatubo. Prior reconstructions of volcanic forcing, for example those[5,42] used in simulations of the last millennium as part of the fifth phase of the Coupled Model Intercomparison Project[43], appear to underestimate the climate impact of extratropical eruptions relative to tropical eruptions (Supplementary Fig. 7). A more accurate reconstruction of the magnitude and timing of past extratropical eruptions, and the optical properties of the associated stratospheric aerosol, may increase the proportion of temperature variability attributable to external forcing.

The strong sensitivity of simulated radiative forcing to the season and injection height of extratropical eruptions—which results from impacts on stratospheric lifetime, aerosol effective radius and phasing between SAOD and incoming solar radiation[27]—is consistent with the scatter in the relationship between tree-ring-derived cooling and VSSI for extratropical eruptions. Reconstructions of volcanic forcing could, therefore, benefit from information of the season and injection height. Information on the eruption season has been obtained, in some cases, from high-resolution analysis of ice cores[44], historical records[20,45] and geochemical analysis of volcanic tephra in ice cores[46–48]. Analysis of the isotopic composition of ice core sulfate has been suggested as indicative of the height reached by the sulfate aerosol[49–51], although this approach has been criticized on the basis that isotopic sulfur fractionation is related to the height of aerosol with respect to the peak in the vertical profile of extratropical ozone concentration rather than with respect to the tropopause[9]. Our model results suggest that aerosol lifetime varies throughout the extratropical lower stratosphere, with an important threshold being the interface between the LMS and overworld, which is comparable to the level of peak ozone concentration. Thus, our results support the utility of sulfur isotope analysis for providing valuable information on volcanic radiative forcing.

Volcanic eruptions with a large VSSI have been less frequent in the extratropics than in the tropics over recent centuries (Fig. 1). Many of the largest ice core sulfate signals from extratropical eruptions originate from eruptions that were at least partly effusive, for example Laki (1783/1784 CE)[52]. In other cases, extratropical eruptions with a large erupted mass, such as Changbaishan (946 CE)[53] appear to have had a small VSSI. A clear example of an extratropical explosive eruption with a strong VSSI is that of the ~536 CE eruption, which produced solar dimming that lasted over a year[54], leading to some of the coldest Northern Hemisphere temperatures of the Common Era. Two thousand years is, however, a short sample in geological terms, and the (admittedly incomplete[55]) Holocene volcanic record[28] suggests major (volcanic explosivity index (VEI) ≥5) eruptions are just as common in the NHET as in the tropics. Extratropical volcanic eruptions with large sulfur injections into the stratospheric overworld have occurred in the past, and they will in the future. Our results suggest that, rather than reducing the radiative forcing and climate impact of such major eruptions, the extratropical eruption latitude acts primarily to focus the radiative impacts within the Northern Hemisphere, which strengthens the hemispheric climate impact.

Online content

Any methods, additional references, Nature Research reporting summaries, source data, statements of data availability and associated accession codes are available at https://doi.org/10.1038/s41561-018-0286-2.

Received: 14 December 2017; Accepted: 4 December 2018;
Published online: 28 January 2019

References

1. Robock, A. Volcanic eruptions and climate. *Rev. Geophys.* **38**, 191–219 (2000).
2. Kirtman, B. et al. in *Climate Change 2013: The Physical Science Basis* (eds Stocker, T. F. et al.) 953–1028 (Cambridge Univ. Press, Cambridge, 2013).
3. Myhre, G. et al. in *Climate Change 2013: The Physical Science Basis* (eds Stocker, T. F. et al.) 658–740 (IPCC, Cambridge Univ. Press, Cambridge, 2013).
4. Schneider, D. P., Ammann, C. M., Otto-Bliesner, B. L. & Kaufman, D. S. Climate response to large, high-latitude and low-latitude volcanic eruptions in the Community Climate System Model. *J. Geophys. Res.* **114**, D15101 (2009).
5. Gao, C., Robock, A. & Ammann, C. Volcanic forcing of climate over the past 1500 years: an improved ice core-based index for climate models. *J. Geophys. Res.* **113**, D23111 (2008).
6. Ammann, C. M., Meehl, G. A., Washington, W. M. & Zender, C. S. A monthly and latitudinally varying volcanic forcing dataset in simulations of 20th century climate. *Geophys. Res. Lett.* **30**, 1657 (2003).
7. Carn, S. A., Clarisse, L. & Prata, A. J. Multi-decadal satellite measurements of global volcanic degassing. *J. Volcanol. Geotherm. Res.* **311**, 99–134 (2016).
8. Sigl, M. et al. Timing and climate forcing of volcanic eruptions for the past 2,500 years. *Nature* **523**, 543–549 (2015).
9. Schmidt, A., Thordarson, T., Oman, L. D., Robock, A. & Self, S. Climatic impact of the long-lasting 1783 Laki eruption: inapplicability of mass-independent sulfur isotopic composition measurements. *J. Geophys. Res.* **117**, D23116 (2012).
10. Santer, B. D. et al. Volcanic contribution to decadal changes in tropospheric temperature. *Nat. Geosci.* **7**, 185–189 (2014).
11. Solomon, S. et al. The persistently variable 'background' stratospheric aerosol layer and global climate change. *Science* **333**, 866–870 (2011).
12. Haywood, J. M., Jones, A., Bellouin, N. & Stephenson, D. Asymmetric forcing from stratospheric aerosols impacts Sahelian rainfall. *Nat. Clim. Change* **3**, 660–665 (2013).
13. Colose, C. M., LeGrande, A. N. & Vuille, M. The influence of volcanic eruptions on the climate of tropical South America during the last millennium in an isotope-enabled general circulation model. *Clim. Past* **12**, 961–979 (2016).
14. Pausata, F. S. R., Chafik, L., Caballero, R. & Battisti, D. S. Impacts of high-latitude volcanic eruptions on ENSO and AMOC. *Proc. Natl Acad. Sci. USA* **112**, 13784–13788 (2015).
15. Stevenson, S., Fasullo, J. T., Otto-Bliesner, B. L., Tomas, R. A. & Gao, C. Role of eruption season in reconciling model and proxy responses to tropical volcanism. *Proc. Natl Acad. Sci. USA* **114**, 1822–1826 (2017).
16. Toohey, M., Krüger, K., Sigl, M., Stordal, F. & Svensen, H. Climatic and societal impacts of a volcanic double event at the dawn of the Middle Ages. *Clim. Change* **136**, 401–412 (2016).
17. Büntgen, U. et al. Cooling and societal change during the Late Antique Little Ice Age from 536 to around 660 AD. *Nat. Geosci.* **9**, 231–236 (2016).
18. Briffa, K. R., Jones, P. D., Schweingruber, F. H. & Osborn, T. J. Influence of volcanic eruptions on Northern Hemisphere summer temperature over the past 600 years. *Nature* **393**, 450–455 (1998).
19. Wilson, R. et al. Last millennium Northern Hemisphere summer temperatures from tree rings. Part I: The long term context. *Quat. Sci. Rev.* **134**, 1–18 (2016).
20. Stoffel, M. et al. Estimates of volcanic-induced cooling in the Northern Hemisphere over the past 1,500 years. *Nat. Geosci.* **8**, 784–788 (2015).
21. Schneider, L. et al. Revising midlatitude summer temperatures back to AD 600 based on a wood density network. *Geophys. Res. Lett.* **42**, 4556–4562 (2015).
22. Toohey, M. & Sigl, M. Volcanic stratospheric sulfur injections and aerosol optical depth from 500 BCE to 1900 CE. *Earth Syst. Sci. Data* **9**, 809–831 (2017).
23. Gao, C., Oman, L., Robock, A. & Stenchikov, G. L. Atmospheric volcanic loading derived from bipolar ice cores: accounting for the spatial distribution of volcanic deposition. *J. Geophys. Res.* **112**, D09109 (2007).
24. Oman, L. et al. Modeling the distribution of the volcanic aerosol cloud from the 1783–1784 Laki eruption. *J. Geophys. Res.* **111**, D12209 (2006).
25. Guo, S., Bluth, G. J. S., Rose, W. I., Watson, I. M. & Prata, A. J. Re-evaluation of SO_2 release of the 15 June 1991 Pinatubo eruption using ultraviolet and infrared satellite sensors. *Geochem. Geophys. Geosyst.* **5**, Q04001 (2004).
26. Toohey, M., Krüger, K., Niemeier, U. & Timmreck, C. The influence of eruption season on the global aerosol evolution and radiative impact of tropical volcanic eruptions. *Atmos. Chem. Phys.* **11**, 12351–12367 (2011).
27. Kravitz, B. & Robock, A. Climate effects of high-latitude volcanic eruptions: role of the time of year. *J. Geophys. Res.* **116**, D01105 (2011).
28. Global Volcanism Program *Volcanoes of the World* v.4.4.1. (ed. Venzke, E.) (Smithsonian Institution, accessed 13 Oct 2015); https://doi.org/10.5479/si.GVP.VOTW4-2013
29. D'Arrigo, R., Wilson, R. & Tudhope, A. The impact of volcanic forcing on tropical temperatures during the past four centuries. *Nat. Geosci.* **2**, 51–56 (2008).
30. Plumb, R. A. Stratospheric transport. *J. Meteorol. Soc. Jpn* **80**, 793–809 (2002).
31. Holton, J. R. et al. Stratosphere–troposphere exchange. *Rev. Geophys.* **33**, 403–439 (1995).
32. Timmreck, C. et al. Aerosol size confines climate response to volcanic super-eruptions. *Geophys. Res. Lett.* **37**, L24705 (2010).
33. Lacis, A. Volcanic aerosol radiative properties. *PAGES Newsl.* **23**, 50–51 (2015).
34. Stenchikov, G. L. et al. Radiative forcing from the 1991 Mount Pinatubo volcanic eruption. *J. Geophys. Res.* **103**, 13837–13857 (1998).
35. Forster, P. M. et al. Recommendations for diagnosing effective radiative forcing from climate models for CMIP6. *J. Geophys. Res. Atmos.* **121**, 12460–12475 (2016).
36. Hansen, J. et al. Efficacy of climate forcings. *J. Geophys. Res.* **110**, D18104 (2005).
37. Shindell, D. & Faluvegi, G. Climate response to regional radiative forcing during the twentieth century. *Nat. Geosci.* **2**, 294–300 (2009).
38. Shindell, D. T., Faluvegi, G., Rotstayn, L. & Milly, G. Spatial patterns of radiative forcing and surface temperature response. *J. Geophys. Res. Atmos.* **120**, 5385–5403 (2015).
39. Glaze, L. S. & Baloga, S. M. Sensitivity of buoyant plume heights to ambient atmospheric conditions: implications for volcanic eruption columns. *J. Geophys. Res.* **101**, 1529–1540 (1996).
40. Sparks, R. S. J. The dimensions and dynamics of volcanic eruption columns. *Bull. Volcanol.* **48**, 3–15 (1986).
41. Hildreth, W. & Fierstein, J. *The Novarupta-Katmai Eruption of 1912—Largest Eruption of the Twentieth Century: Centennial Perspective*s US Geological Survey Professional Paper 1791 (US Geological Survey, 2012).
42. Crowley, T. J. & Unterman, M. B. Technical details concerning development of a 1200 yr proxy index for global volcanism. *Earth Syst. Sci. Data* **5**, 187–197 (2013).
43. Schmidt, G. A. et al. Climate forcing reconstructions for use in PMIP simulations of the last millennium (v1.0). *Geosci. Model Dev.* **4**, 33–45 (2011).
44. Cole-Dai, J. et al. Cold decade (AD 1810–1819) caused by Tambora (1815) and another (1809) stratospheric volcanic eruption. *Geophys. Res. Lett.* **36**, L22703 (2009).
45. Guillet, S. et al. Climate response to the Samalas volcanic eruption in 1257 revealed by proxy records. *Nat. Geosci* **10**, 123–128 (2017).
46. Jensen, B. J. L. et al. Transatlantic distribution of the Alaskan White River Ash. *Geology* **42**, 875–878 (2014).
47. Sun, C. et al. Ash from Changbaishan Millennium eruption recorded in Greenland ice: implications for determining the eruption's timing and impact. *Geophys. Res. Lett.* **41**, 694–701 (2014).
48. Oppenheimer, C. et al. The Eldgjá eruption: timing, long-range impacts and influence on the Christianisation of Iceland. *Clim. Change* **147**, 369–381 (2018).
49. Baroni, M., Savarino, J., Cole-Dai, J., Rai, V. K. & Thiemens, M. H. Anomalous sulfur isotope compositions of volcanic sulfate over the last millennium in Antarctic ice cores. *J. Geophys. Res.* **113**, D20112 (2008).
50. Savarino, J., Romero, A., Cole-Dai, J., Bekki, S. & Thiemens, M. H. UV induced mass-independent sulfur isotope fractionation in stratospheric volcanic sulfate. *Geophys. Res. Lett.* **30**, 2131 (2003).

51. Lanciki, A., Cole-Dai, J., Thiemens, M. H. & Savarino, J. Sulfur isotope evidence of little or no stratospheric impact by the 1783 Laki volcanic eruption. *Geophys. Res. Lett.* **39**, L01806 (2012).
52. Thordarson, T. & Larsen, G. Volcanism in Iceland in historical time: volcano types, eruption styles and eruptive history. *J. Geodyn.* **43**, 118–152 (2007).
53. Oppenheimer, C. et al. Multi-proxy dating the 'Millennium Eruption' of Changbaishan to late 946 CE. *Quat. Sci. Rev.* **158**, 164–171 (2017).
54. Stothers, R. B. Mystery cloud of AD 536. *Nature* **307**, 344–345 (1984).
55. Watt, S. F. L., Pyle, D. M. & Mather, T. A. The volcanic response to deglaciation: evidence from glaciated arcs and a reassessment of global eruption records. *Earth Sci. Rev.* **122**, 77–102 (2013).

Acknowledgements

This work was supported by the Federal Ministry for Education and Research in Germany (BMBF) through the research program "MiKlip" (grant nos FKZ:01LP130B, 01LP1130A and 01LP1517B). M.T. additionally acknowledges support by the Deutsche Forschungsgemeinschaft (DFG) in the framework of the priority programme "Antarctic Research with comparative investigations in Arctic ice areas" through grant no. TO 967/1-1. K.K. and M.Sigl acknowledge support through the NFR project "VIKINGS" (project no. 275191). C.T. additionally acknowledges support from the European Union project StratoClim (FP7-ENV.2013.6.1-2). Computations were performed at the German Climate Computer Center (DKRZ). The authors thank L. Schneider and co-workers for making their Northern Hemisphere temperature reconstruction publically available. This paper is a product of the Volcanic Impacts on Climate and Society (VICS) working group, as part of the Past Global Changes (PAGES) project, which in turn received support from the US National Science Foundation and the Swiss Academy of Sciences.

Author contributions

M.T., K.K., C.T. and H.S. designed the model experiments. M.T. performed the model simulations and analysis with input from K.K., C.T. and H.S. M.T. performed the analysis of the tree-ring-temperature reconstructions and VSSIs with input from M.Sigl, M.Stoffel and R.W. M.T. led the manuscript writing with input from all the co-authors.

Competing interests

The authors declare no competing interests.

Additional information

Supplementary information is available for this paper at https://doi.org/10.1038/s41561-018-0286-2.

Reprints and permissions information is available at www.nature.com/reprints.

Correspondence and requests for materials should be addressed to M.T.

Methods

Sulfur injections. VSSI estimates before 1900 CE are taken from the eVolv2k database[22], based on analysis of bipolar ice core arrays. For the twentieth century, satellite observations[7] are used for estimates of VSSI for Pinatubo (1991) and El Chichón (1982). For eruptions between 1900 and the start of the satellite era, we used Antarctic and Greenland ice core sulfate fluxes from the ice core index reconstruction of Crowley and Unterman[42], and applied the scaling methodology used in the construction of eVolv2k. Categorization of the eruptions as tropical or extratropical is provided by the eVolv2k reconstruction based on the presence or lack of bipolar ice core sulfate signals, or from observations for twentieth century eruptions. Eruption years for unidentified tropical eruptions are adjusted to one year earlier than listed in the eVolv2k database to account for the typical one-year lag between eruption and ice sheet deposition. All the unidentified eruptions are thereafter assumed to have a dating uncertainty of ±1 yr for 1750–1900 CE and ± 2 yr from 500 to 1750 CE.

Posteruption Northern Hemisphere temperature anomalies. Based on the compiled VSSI record, we first selected tropical and Northern Hemisphere extratropical volcanic events between 500 and 2000 CE with an estimated VSSI greater than 2 TgS. From this list, to exclude events in which cooling from the eruption in question may be superimposed on the return to normal conditions after a preceding eruption, we exclude events for which an eruption of magnitude greater than 2 TgS occurred within the preceding six years, and also those for which an event greater than 10 TgS occurred within the preceding ten years. This process excluded 17 eruptions (Supplementary Table 1), which include well-known examples such as Tambora (1815) and an unidentified eruption of ~1457 CE. Extratropical eruptions that are known or suspected to have been characterized by some degree of effusive eruption style, which include the strong Icelandic 'fire' eruptions of Laki (1783–1784) and Eldgjá (939) are also excluded (Supplementary Table 2). The remaining extratropical events are assumed to represent extratropical explosive events, although it should be clear that this list probably includes signals from additional Icelandic effusive events.

For each volcanic event, Northern Hemisphere summer temperature anomalies were constructed using three recent reconstructions[19–21]. First, based on a simple mean of the three reconstructions, eruption dates for unidentified eruptions were adjusted within the dating uncertainty to maximize the post-eruption 3 yr mean cooling anomaly. This adjustment aims to take into account uncertainty in the dating of the ice core signals, but also the possible shift related to eruptions that occurred before or after the summer of any calendar year. Temperature anomalies for each event and each temperature reconstruction were then calculated with respect to the preceding 5 yr. Given an estimated eruption at year y_0, Northern Hemisphere 3 yr mean temperature anomalies ($\Delta T_{3\mathrm{yr}}$) were calculated as follows for tropical and Northern Hemisphere extratropical eruptions, respectively:

$$\Delta T_{3\mathrm{yr}} = \frac{1}{3}\sum_{i=1}^{3} T_{y_0+i} - \frac{1}{5}\sum_{i=-5}^{-1} T_{y_0+i}$$

$$\Delta T_{3\mathrm{yr}} = \frac{1}{3}\sum_{i=0}^{2} T_{y_0+i} - \frac{1}{5}\sum_{i=-5}^{-1} T_{y_0+i}$$

Uncertainties (σ) in the tree-ring-based temperature reconstructions are taken from the original data sets. Uncertainties in postvolcanic 3 yr temperature anomalies and multireconstruction means are calculated using reported uncertainties and standard rules of error propagation.

MAECHAM5-HAM. Volcanic simulations were performed with the aerosol-climate model MAECHAM5-HAM[26,56,57]. The spatial resolution was ~2.8° by 2.8°, with a T42 spectral truncation and 39 vertical levels up to 0.01 hPa (~80 km). The atmospheric component of the model was free running, whereas SSTs were prescribed as an annually repeating climatology.

Simulations were initiated by the injection of SO_2 into a specified model grid box and height. A sulfur chemistry module converts SO_2 into H_2SO_4 via the reactions:

$$SO_2 + OH + M \rightarrow HSO_3 + M \tag{1}$$

$$HSO_3 + O_2 \rightarrow HO_2 + SO_3 \tag{2}$$

$$SO_3 + H_2O \rightarrow H_2SO_4 \tag{3}$$

The rate of SO_2 to H_2SO_4 conversion depends on the concentrations of the OH taken from prior chemistry–climate model simulations[58]. The use of prescribed OH concentrations neglects potential changes in H_2SO_4 production rates due to the local consumption of OH, which is thought to play an important role for extremely large eruptions[59]. The prescribed monthly mean OH fields contain a significant spatial structure (Supplementary Fig. 5), with very low concentrations in polar winter due to the dependence of OH production on solar insolation. There is also a strong vertical gradient in OH concentrations through the lower and middle stratosphere, due to changes in the solar ultraviolet radiative flux and the availability of H_2O, which has a minimum around the level of the tropopause.

After oxidation of the volcanic SO_2 source gas, H_2SO_4 condenses with water to form sulfate (SO_4) aerosol. Aerosol processes in MAECHAM5-HAM were calculated by the aerosol microphysical module HAM[60], and include aerosol formation and growth via nucleation, condensation, accumulation and coagulation, then vertical redistribution via sedimentation and finally the removal processes of wet and dry deposition.

Pinatubo-magnitude simulations with MAECHAM5-HAM resulted in a good agreement with observations in terms of the aerosol optical depth, top of atmosphere short-wave radiation anomalies, and aerosol effective radius[26,56]. The MAECHAM5-HAM configuration used here has no quasi-biennial oscillation: winds in the equatorial stratosphere are easterly throughout the year, and therefore the variability of stratospheric dynamics[61] and aerosol transport related to the quasi-biennial oscillation are not included in the simulations. The decay of simulated aerosol optical depth was found to be slightly faster than that observed, which is perhaps related to a slight high bias in the simulated aerosol effective radius[56]. However, consistency in the timing of the extratropical aerosol optical depth peak values suggests the model reproduces well the seasonal variation in aerosol transport[26]. For the tropical eruptions of Pinatubo magnitude and less, the model produces a linear relationship between radiative forcing and VSSI[62].

Model experiments. To isolate the impact of eruption latitude on the aerosol evolution and resulting radiative forcing, we performed ensemble MAECHAM5-HAM simulations with a fixed magnitude of VSSI at various latitudes, months and injection heights. We chose the estimated VSSI of the 1991 eruption of Pinatubo (17 $TgSO_2$ or, equivalently, 8.5 TgS injection), because observations of the Pinatubo aerosol provide the best estimates of sulfur injection, aerosol evolution and radiative forcing of any major volcanic eruption, which makes it a standard modelling validation experiment. Simulation eruption locations were chosen based on the global distribution of identified volcanic eruptions with VEI equal to or greater than 5 (Supplementary Fig. 2) according to the Volcanoes of the World database[28]. Four 10° latitude ranges contain 57% of all the VEI ≥ 5 eruptions in the Volcanoes of the World database: in the order of eruption frequency, these latitude bands are 50–60° N, 30–40° N, 0–10° S and 10–20° N. For each of these four latitude ranges, we chose a 'typical' eruption location, roughly consistent with the highest density of identified eruptions, sampling global eruptions hot spots that included Indonesia, Central America, Japan and Alaska (Supplementary Table 6). The chosen eruption locations are spread evenly between the western and eastern coasts of the Pacific Ocean, although model simulations suggest no significant impact of the eruption longitude on the aerosol evolution after explosive tropical eruptions[26]. To include the potential impacts of eruption season, simulations were performed with eruptions in both January and July. This choice of months is somewhat arbitrary, but is motivated by: (1) the common use of 1 January as a standard eruption date for eruptions of unknown eruption timing in volcanic forcing reconstructions[22,42], (2) the rough agreement of 1 July with the actual seasonal timing of the Pinatubo eruption (on June 15, 1991) and (3) the fact that Northern Hemisphere radiative anomalies from January and July tropical eruptions nearly span the full range of SAOD and radiative forcing seen in model simulations using a fuller sample of eruption season distribution[26]. As the spatial spread of aerosol is sensitive to the meteorological conditions at the time of the eruption[63], ensembles of simulation were performed. For each of the four eruption locations, we performed ten MAECHAM-HAM eruption simulations with a SO_2 injection at 30 hPa (~23 km), five simulations each for injections in January and July. To investigate the impact of injection height for extratropical eruptions, simulations at 56°N were repeated with injection heights of 100 hPa (~16 km) and 150 hPa (~13 km) with, again, five simulations for January eruptions, and five simulations for July eruptions.

A 30 yr control run was performed with no stratospheric sulfur injections, with all other boundary conditions and forcings identical to the eruption simulations.

Model output. Sulfate aerosol column burdens and SAOD were output directly by the model, and zonal means over the full globe and the NHET values were calculated using area-weighted means. Stratospheric sulfur e-folding lifetimes were calculated as the time taken for the total sulfur burden ($SO_2 + H_2SO_4$) to cross $1/e$ of the injected amount, where e is the mathematical constant approximately equal to 2.71828. Lifetime based on total sulfur is typically longer than that calculated based on the decay of sulfate after its peak value, but is a better measure of the efficiency of loss processes because the timing of the sulfate peak also depends on the rate of SO_2-to-H_2SO_4 conversion. Sulfate aerosol effective radius (r_{eff}), a function of height, latitude and longitude, was averaged in space using sulfate aerosol mass as a weighting function. The resulting sulfate-mass-weighted $\langle r_{\mathrm{eff}} \rangle$ represents the typical r_{eff} in the region of the most sulfate aerosol, which will dominate the radiative transfer calculations. Net (shortwave + longwave) top of atmosphere radiative anomalies were calculated as the difference radiative fluxes between each eruption simulation and the control run climatology, which corresponds to the 'fixed SST' ERF quantity[35,36].

Code availability

The Matlab scripts used for the analyses described in this study can be obtained from the corresponding author upon reasonable request.

Data availability

The VSSI estimates used in this study are available in the World Data Center for Climate hosted by the German Climate Computing Center (DKRZ) with the identifier https://doi.org/10.1594/WDCC/eVolv2k_v2. The Northern Hemisphere temperature reconstructions used are available from the NOAA/World Data Service for Paleoclimatology archives via the links https://www.ncdc.noaa.gov/paleo-search/study/19743, https://www.ncdc.noaa.gov/paleo-search/study/19039 and https://www.ncdc.noaa.gov/paleo-search/study/18875. Output from the MAECHAM5-HAM simulations is available from the corresponding author upon reasonable request.

References

56. Niemeier, U. et al. Initial fate of fine ash and sulfur from large volcanic eruptions. *Atmos. Chem. Phys.* **9**, 9043–9057 (2009).
57. Toohey, M., Krüger, K. & Timmreck, C. Volcanic sulfate deposition to Greenland and Antarctica: a modeling sensitivity study. *J. Geophys. Res. Atmos.* **118**, 4788–4800 (2013).
58. Timmreck, C., Graf, H.-F. & Steil, B. in *Volcanism and the Earth's Atmosphere* (eds Robock, A. & Oppenheimer, C.) 213–225 (Geophysical Monograph Series Vol. 139, American Geophysical Union, 2003).
59. Bekki, S. Oxidation of volcanic SO_2: a sink for stratospheric OH and H_2O. *Geophys. Res. Lett.* **22**, 913–916 (1995).
60. Stier, P. et al. The aerosol–climate model ECHAM5-HAM. *Atmos. Chem. Phys.* **5**, 1125–1156 (2005).
61. Punge, H. J., Konopka, P., Giorgetta, M. A. & Müller, R. Effects of the quasi-biennial oscillation on low-latitude transport in the stratosphere derived from trajectory calculations. *J. Geophys. Res.* **114**, D03102 (2009).
62. Metzner, D. et al. Radiative forcing and climate impact resulting from SO_2 injections based on a 200,000-year record of Plinian eruptions along the Central American Volcanic Arc. *Int. J. Earth Sci.* **103**, 2063–2079 (2014).
63. Jones, A. C., Haywood, J. M., Jones, A. & Aquila, V. Sensitivity of volcanic aerosol dispersion to meteorological conditions: a Pinatubo case study. *J. Geophys. Res. Atmos.* **121**, 6892–6908 (2016).